Monthly Notices
of the
ROYAL ASTRONOMICAL SOCIETY

MNRAS **541,** 3518–3533 (2025)
Advance Access publication 2025 July 3

https://doi.org/10.1093/mnras/staf1085

Joint radiative and kinematic modelling of X-ray binary ejecta: energy estimate and reverse shock detection

A. J. Cooper,[1★] J. H. Matthews,[1] F. Carotenuto,[1,2] R. Fender,[1,3] G. P. Lamb,[4] T. D. Russell,[5] N. Sarin,[6,7] K. Savard[1] and A. A. Zdziarski[8]

[1]*Astrophysics, The University of Oxford, Keble Road, Oxford OX1 3RH, UK*
[2]*INAF – Osservatorio Astronomico di Roma, Via Frascati 33, I-00078 Monte Porzio Catone (RM), Italy*
[3]*Department of Astronomy, University of Cape Town, Private Bag X3, Rondebosch 7701, South Africa*
[4]*Astrophysics Research Institute, Liverpool John Moores University, IC2 Liverpool Science Park, 146 Brownlow Hill, Liverpool L3 5RF, UK*
[5]*INAF, Istituto di Astrofisica Spaziale e Fisica Cosmica, Via U. La Malfa 153, I-90146 Palermo, Italy*
[6]*Oskar Klein Centre, Department of Physics, Stockholm University, Albanova University Center, SE 106 91 Stockholm, Sweden*
[7]*Nordita, Stockholm University and KTH Royal Institute of Technology, Hannes Alfvéns väg 12, SE-106 91 Stockholm, Sweden*
[8]*Nicolaus Copernicus Astronomical Center, Polish Academy of Sciences, Bartycka 18, PL-00-716 Warszawa, Poland*

Accepted 2025 June 30. Received 2025 June 26; in original form 2025 March 12

ABSTRACT

Black hole X-ray binaries in outburst launch discrete, large-scale jet ejections, which can propagate to parsec scales. The kinematics of these ejecta appear to be well described by relativistic blast wave models originally devised for gamma-ray burst afterglows. In previous kinematic-only modelling, a crucial degeneracy prevented the initial ejecta energy and the interstellar medium density from being accurately determined. In this work, we present the first joint Bayesian modelling of the radiation and kinematics of a large-scale jet ejection from the X-ray binary MAXI J1535−571. We demonstrate that a reverse shock powers the bright, early ejecta emission. The joint model breaks the energetic degeneracy, and we find the ejecta has an initial energy of $E_0 \sim 3 \times 10^{43}$ erg, and propagates into a low density interstellar medium of $n_{\rm ism} \sim 4 \times 10^{-5}\,{\rm cm}^{-3}$. The ejecta is consistent with being launched perpendicular to the disc and could be powered by an efficient conversion of available accretion power alone. This work lays the foundation for future parameter estimation studies using all available data of X-ray binary jet ejecta.

Key words: acceleration of particles – shock waves – gamma-ray burst: general – ISM: jets and outflows – radio continuum: transients – X-rays: binaries.

1 INTRODUCTION

Astrophysical jets are observed ubiquitously from accreting compact objects across a variety of spatial scales. Supermassive black holes (BHs) at the centres of galaxies power Mpc-scale jets (e.g. Blandford, Meier & Readhead 2019), which evolve on Myr time-scales and whose feedback appears to regulate galactic growth (e.g. Ferrarese & Merritt 2000). Stellar-mass BHs can accrete rapidly after their formation to power gamma-ray bursts (GRBs) or more slowly from companion stars through winds or Roche lobe overflow as BH X-ray binaries (XRBs).

BH-XRBs are binary systems in which stellar-mass BHs ($M_{\rm BH} \lesssim 20\,{\rm M}_{\odot}$) accrete from a companion star. BH-XRBs are typically identified by wide-field X-ray instruments during outbursts likely triggered by disc instabilities (e.g. Lasota 2001). During outburst, BH-XRBs cycle through X-ray states on time-scales of days–months (Remillard & McClintock 2006). Canonically (see e.g. Fender, Belloni & Gallo 2004), these sources begin in quiescence before entering the hard state upon outburst onset, characterized by hard spectrum X-ray emission ($L_{\rm X} \lesssim 0.1 L_{\rm Edd}$) and a partially absorbed compact, steady radio jet with a flat spectral index. The X-ray luminosity increases ($L_{\rm X} \gtrsim 0.1 L_{\rm Edd}$), before the X-ray spectrum begins to soften and the source enters a bright intermediate phase. The softening of the X-ray emission is marked by dramatic changes in the jet (Fender, Homan & Belloni 2009), where the compact jet is quenched, bright self-absorbed radio flares are produced, and large-scale relativistic ejecta are launched along the jet axis. These ejecta are observed as discrete knots of optically thin, synchrotron-emitting ‘blobs’ of plasma. The source will usually enter the soft state, during which no compact jet emission is detected, and the X-ray luminosity begins to decrease. The source transitions back to the hard state as the X-ray luminosity usually continues to fade towards quiescence. During this reverse soft-to-hard transition, observations are consistent with no further ejecta being launched; instead, the compact jet is gradually re-established upon return to the hard state (e.g. Russell et al. 2014). The production and propagation of the relativistic jet ejecta during the hard–soft transition are the focus of this work.

Bipolar jet ejections from the BH-XRB GRS 1915 + 105 were identified by Mirabel & Rodríguez (1994) as the first apparently superluminal Galactic sources. The advent of large-scale GHz

---

★ E-mail: alexander.cooper@physics.ox.ac.uk

radio interferometers has, through dedicated programmes such as ThunderKAT (Fender et al. 2016), enabled the regular detection and tracking of discrete ejecta as they propagate out to large distances from the core. Sixteen such sources now have discrete ejecta resolved from the core at either radio or X-ray frequencies (Mirabel & Rodríguez 1994; Hjellming et al. 2000; Hannikainen et al. 2001; Mioduszewski et al. 2001; Corbel et al. 2002, 2005; Gallo et al. 2004; Yang et al. 2010; Rushton et al. 2017; Miller-Jones et al. 2019; Russell et al. 2019; Bright et al. 2020; Carotenuto et al. 2021; Williams et al. 2022; Bahramian et al. 2023; Wood et al. 2023; Zhang et al. 2025), with a subset tracked continuously to core-offsets of tens of arcseconds. However, theoretical interpretation and modelling of the excellent available data has been somewhat limited. The first model of BH-XRB ejecta was pioneered by Wang, Dai & Lu (2003) via adaptation of the kinematic GRB model from Huang, Dai & Lu (1999) to fit the eastern jet of XTE J1550−564. That model seeks to conserve the conical jet's energy as it sweeps up mass and decelerates:

$$E_0 = (\Gamma - 1)M_0c^2 + \sigma(\Gamma_{\rm sh} - 1)m_{\rm sw}c^2, \tag{1}$$

where E_0 and M_0 are the jet's initial energy and mass, respectively, $m_{\rm sw}(t)$ is the swept-up mass, σ is the adiabatic index (interpolated between ultrarelativistic and non-relativistic values), and $\Gamma(t)$ and $\Gamma_{\rm sh}(t)$ are the Lorentz factors of the jet material and shock front, respectively. Wang et al. (2003) inferred that a low interstellar medium (ISM) density (also known as the circumburst density) is required to explain the observed propagation of the ejecta from XTE J1550−564, indicative of parsec-scale underdense cavities in the environment surrounding the source. The authors further modelled the X-ray emission of the ejecta, followed by similar modelling of both the approaching and receding jets by Hao & Zhang (2009). In their work, Wang et al. (2003) find that a forward shock model evolved too slowly to explain the observed X-ray flux, but a reverse shock fit the data relatively well.

Since these seminal works, modelling attempts have exclusively focused on the kinematics of XRB jets. Steiner & McClintock (2012) used a conical jet model to further study the jet kinematics of XTE J1550−564, allowing them determine a jet inclination angle ($\theta_{\rm obs}$) of ~ 71 deg. The same methodology was used by Steiner, McClintock & Reid (2012) to determine a distance and inclination angle for double-sided jets of H1743−322. Carotenuto, Tetarenko & Corbel (2022) recently adapted this model to include a sharp density jump representing the edge of the underdense cavity surrounding MAXI J1348−630 in their modelling of jet kinematics, although Zdziarski et al. (2023) showed that a smooth cavity transition explains the observations while alleviating energetic requirements. Carotenuto et al. (2024) applied the same kinematic model to three more XRB sources with large-scale ejecta: MAXI J1820 + 070, MAXI J1535−571, and XTE J1752−223. The authors were able to determine jet launching times, initial Lorentz factors, and upper limits to the ISM density, $n_{\rm ism}$, by comparing degenerate energy estimates to available accretion power over launching time-scales inferred by radio flare durations. However, these kinematic-only, conical jet models have a key degeneracy between the initial energy E_0, the half-opening angle $\theta_{\rm c}$, and the density of the ISM. This means that usually only a degenerate quantity known as the 'effective energy' $E_{0,\rm eff} = E_0 n_{\rm ism}^{-1}(\theta_{\rm c})^{-2}$ can be derived (Carotenuto et al. 2024), unless one or more of these quantities is measured by other means. Finally, Sarath & Böttcher (2025) utilized a kinematic model similar to Zdziarski et al. (2023) to model the ejecta from MAXI J1348−630, while employing a modified blazar model to predict the radiative properties. Their model successfully explains the late-time radio rebrightening of the ejecta upon ejecta-cavity interaction, but does not capture the early-time flux which we attribute in this work to a reverse shock.

Interpreting the full wealth of excellent data from BH-XRB jets is crucial to better understand their nature. The supreme data quality, owing to proximity and evolution on human-accessible time-scales, probes the propagation and deceleration in detail, enabling a unique view of macrophysical blastwave physics and the microphysics of particle acceleration in jets (Matthews et al. 2025). Furthermore, excellent prior observational constraints, particularly of jet opening angles, distances, and BH properties, greatly enhance modelling capabilities. This is particularly important in order to verify long-standing notions that we may be greatly underestimating the true energetics of BH-XRB jets (Gallo et al. 2005) and that BH-XRBs are surrounded by underdense cavities (Heinz 2002; Hao & Zhang 2009; Carotenuto et al. 2022, 2024; Savard et al. 2025). More accurate determinations of the initial jet energies will also help quantify their importance as a Galactic feedback mechanism (Heinz & Sunyaev 2002; Heinz, Merloni & Schwab 2007; Heinz et al. 2008) and as a significant source of high-energy cosmic rays and neutrinos (Fender, Maccarone & van Kesteren 2005; Cooper et al. 2020; Kimura et al. 2021; Kantzas et al. 2023; Kuze, Kimura & Fang 2025; Bacon et al. in preparation). The latter is of particular relevance given recent detections of ultra high-energy (> 100 TeV) gamma-rays from a number of BH-XRBs (LHAASO Collaboration 2024), in addition to earlier detections of very high energy (> 100 GeV) gamma-rays (Aharonian et al. 2005; Albert et al. 2006, 2007; Abeysekara et al. 2018). Finally, a better understanding of Galactic BH jets may enable us to better characterize other jetted sources including GRBs, tidal disruption events, and active galactic nuclei, where similar (often scale-invariant) physics dictates jet propagation and particle acceleration.

In this work, we present the first combined radiative and kinematic modelling with Bayesian parameter estimation through a case study of jet ejecta observed from a BH-XRB, MAXI J1535−571. In Section 2, we discuss the MAXI J1535−571 system. In Section 3, we discuss the model, the data selection, and the fitting procedure, including our choice of prior. In Section 4, we present our results, which we discuss in Section 5. We present our primary conclusions and future outlook in Section 6. In Appendix A, we include further discussion on the jet inclination angle of MAXI J1535−571, and in Appendix C we include additional diagnostic plots.

2 MAXI J1535−571

MAXI J1535−571 (henceforth MAXI J1535) is a BH-XRB, discovered after going into outburst in 2017 September (Negoro et al. 2017; Nakahira et al. 2018; Tao et al. 2018) by the Monitor of All-sky X-ray Image (MAXI; Matsuoka et al. 2009) and the SWIFT Burst Alert Telescope (Swift/BAT; Gehrels et al. 2004). The outburst was followed across the electromagnetic spectrum in X-ray (Huang et al. 2018; Miller et al. 2018; Nakahira et al. 2018; Parikh et al. 2019; Sreehari et al. 2019; Dong et al. 2022), optical/infrared (Dincer 2017; Russell et al. 2017; Vincentelli et al. 2021), and radio/sub-mm (Russell et al. 2017, 2019, 2020; Chauhan et al. 2021).

We chose to apply this new joint modelling technique to MAXI J1535 primarily due to the wealth of data on the transient ejecta and the observational constraints available on the source. Russell et al. (2019, 2020) presented a dedicated radio campaign using ATCA (Australia Telescope Compact Array) and MeerKAT ('More' Karoo Array Telescope), tracking the discrete jet ejection (labelled S2 in their work) for over 300 d. The high-spatial resolution of the instrumentation enabled the authors to resolve the core-ejecta separation providing ejecta flux measurements that were uncontaminated from the core emission.

The authors fit the proper motion to constrain the launch date of the ejecta to between MJD 58001.7 and MJD 58026.7 depending on whether the ejecta motion is uniform or decelerating. Carotenuto et al. (2024) fit a conical blastwave model to the kinematic data presented in Russell et al. (2019), constraining the ejecta launch date to MJD $58017.4^{+4.0}_{-3.8}$, the initial Lorentz factor to $\Gamma_0 = 1.6^{+0.2}_{-0.2}$, and the effective energy to $E_{0,\mathrm{eff}} = 5.8^{+16.6}_{-4.0} \times 10^{48}\,(n_{\mathrm{ism}}/1\,\mathrm{cm}^{-3})\,(\theta_{\mathrm{c}}/1\,\mathrm{deg})^{-2}$ erg. We note that this ejection date overlaps with the peak in the X-ray light curve (Shang et al. 2019) and the possible detection of Type-B quasi-periodic oscillations (QPOs) reported by Stevens et al. (2018) from stacked NICER data across MJD 58016.8–58025. Type-B QPOs are thought to be possibly associated with transient jet launching (see e.g. Motta 2016; Ingram & Motta 2019; Wood et al. 2021) and support an ejection date at least in the latter third of the 15-d window reported by Russell et al. (2019), consistent with the launch date derived by Carotenuto et al. (2024). Chauhan et al. (2021) presented quasi-simultaneous broadband radio observations spanning 117 MHz–19 GHz from MJD 58016–58040, spanning the jet ejecta launch and early evolution. The authors interpret their observations as flaring events associated with the launching of discrete ejecta and as possible fading emission from the ejecta. Improved the spatial resolution of observations over this time may distinguish between these scenarios, although we note that the emission fades by MJD 58030, so while it is probably associated with the same material that goes on to produce the large-scale ejecta, it is unlikely *in situ* particle acceleration has begun. Finally, Chauhan et al. (2019) carried out observations of HI absorption spectrum, determining a best-fitting distance to the source of $4.1^{+0.6}_{-0.5}$ kpc, with a robust upper limit at $6.7^{+0.1}_{-0.2}$ kpc, and a lower limit of 3.6 kpc.

2.1 On the inclination angle of the disc and jets of MAXI J1535

X-ray measurements of disc reflection features were carried out on data obtained by various facilities using `XSPEC` (Arnaud 1996). NICER observations of the production region of narrow Fe K emission line using `relline` model imply an inclination angle of $\theta_{\mathrm{obs}} = 37^{+22}_{-13}$ deg, yet in the same work fits of an absorbed disc blackbody component with a relativistically blurred reflection using the `relxill` model find an angle of $\theta_{\mathrm{obs}} = 67.4(8)$ deg (Miller et al. 2018). NuSTAR observations found two models provided satisfactory fits to the data (`xillverCp` and `relxillCp`) with derived inclination angles of $\theta_{\mathrm{obs}} = 57^{+2}_{-1}$ and $\theta_{\mathrm{obs}} = 75^{+4}_{-2}$ deg, respectively (Xu et al. 2018). Finally, a joint NuSTAR and HXMT analysis by Dong et al. (2022) derived a best-fitting inclination angle of the inner accretion disc of $\sim 70 - 74$ deg across all data sets. Broadly, these results typically required large inclination angles $\theta_{\mathrm{obs}} > 45$ deg.

Russell et al. (2019) present constraints on the viewing angle of the transient ejecta, finding $\theta_{\mathrm{obs}} < 45$ deg. The authors use the maximum measured proper motion of 47.2 mas day^{-1}, and solve for families of solutions in θ_{obs} and β for various distances measurements compatible with results of Chauhan et al. (2019). They use the standard equation for superluminal motion (Rees 1966; Mirabel & Rodríguez 1994):

$$\mu_{\mathrm{app}} = \frac{\beta\sin(\theta_{\mathrm{obs}})}{1-\beta\cos(\theta_{\mathrm{obs}})}\frac{c}{D}. \qquad (2)$$

Solutions compatible with the observed proper motion are depicted in their fig. 9, and appear in tension with X-ray disc inclination measurements. This led the authors to posit disc warping, or a possible disc–jet misalignment in MAXI J1535. In our re-analysis, we derived an extension to the acceptable family of solutions above $\theta_{\mathrm{obs}} = 45$ deg, which can reproduce the required proper motion. This re-analysis considerably weaken previous constraints, to $\theta_{\mathrm{obs}} < 76$ degrees for a distance of 4.7 kpc, but unconstrained for the closest distance considered of 3.6 kpc. For this reason, we consider a prior for θ_{obs} encompassing the full 0–90 deg. Further details are provided in the Appendix A.

3 JOINT RADIATIVE AND KINEMATIC MODEL

3.1 Ejecta model

To model both the radiation and kinematics of the discrete ejecta, we utilize `jetsimpy`[1] (Wang et al. 2024). `jetsimpy` is an efficient, reduced hydrodynamic code that approximates the blast wave as an axisymmetric, infinitely thin, 2D surface. Primarily designed for modelling GRB afterglows, `jetsimpy` produces light curves and kinematic profiles for transrelativistic outflows, calibrated to self-similar, ultrarelativistic (Blandford & McKee 1976), and Newtonian (Sedov 1959) blast-wave solutions, making it suitable for XRB ejecta. For the kinematic modelling, we compute at each time t the angular separation of the ejecta from the core using the `jet.Offset` function. We note that while this separation only solves for the forward shock, at early times when emission is dominated by the reverse shock, the forward and reverse shocks are likely co-located (see also Section 5.6 and Matthews et al. 2025).

For the radiation modelling, we compute the emission from the forward shock utilizing `jetsimpy`'s deep-Newtonian synchrotron `sync_dnp` radiation model (Sironi & Giannios 2013). This choice is made over the default `sync` model, as it has been shown to more faithfully reproduce late-time flattening of GRBs (Sironi & Giannios 2013) and to provide better fits to late-time light curve of the GW170817 afterglow (Ryan et al. 2024). These deep Newtonian corrections, which modify the temporal decay of radio flux, are particularly important to include for XRBs due to their generally lower Γ blast waves as compared to GRBs.

For the reverse shock emission, we construct a custom radiation model within `jetsimpy`. We adopt the thin reverse shock model of Kobayashi (2000) (also see section 3.1.2 of Gao et al. 2013), as it is more appropriate than thick shock models for lower Lorentz factors, expected for mildly relativistic XRB ejecta. We additionally correct the canonical (ultrarelativistic) reverse shock crossing timescale to account for moderate initial Lorentz factors (equation 17 in Matthews et al. 2025). We compute first the expected on-axis flux in this regime, taking into account all relevant hierarchies of critical frequencies, where ν_{m} is the synchrotron minimum frequency, ν_{a} is the synchrotron self-absorption frequency, and ν_{c} is the cooling frequency. We transform the on-axis observer-frame flux into the co-moving ejecta frame to calculate a deboosted flux ($F_{\nu,\mathrm{co-moving}}(t) \approx F_{\nu,\theta_{\mathrm{obs}}=0}(t)/(2\Gamma(t))^3$), before dividing through by the forward shock volume as calculated by `jetsimpy` to obtain an emissivity. A crucial assumption here is that the forward and reverse shock widths are equivalent ($\delta R_{\mathrm{FS}} \sim \delta R_{\mathrm{RS}}$). We examine this assumption in Model (A6) in which we fit for a ‘filling factor’ parameter $f = \delta R_{\mathrm{RS}}/\delta R_{\mathrm{FS}}$. The observer-frame flux density is calculated from this emissivity,

---

[1] https://jetsimpy.readthedocs.io

which takes into account the observer viewing angle, photon time-of-arrival effects, and optional jet-spreading (lateral jet expansion to regions $\theta > \theta_c$). Note that we omit order unity numerical correction coefficients derived by Harrison & Kobayashi (2013). This may lead to a slight overestimate of the reverse shock flux, however, given the ejecta's low bulk Γ, this correction is expected to be nominal.

3.2 Data selection

We fit the model to the radio data of the jet ejection 'S2' presented by Russell et al. (2019). We use all 12 core separation datapoints in their table 5 for the kinematic modelling. Errors quoted for separation datapoints are statistical only, thus for simplicity we assign additional conservative 5 per cent errors to each to approximate the systematic error.[2] For the flux measurements, we use all 67 datapoints including non-detections of the ejecta. For the uncertainties, we use the 1σ errors included for detections, and non-detections are three times the root-mean square (rms) of the image noise. We do not include early-time observations (MJD 58000–58050) reported by Chauhan et al. (2021) as these data, taken prior to the detection of distinct ejecta component S2, may be contaminated by emission from the core. Furthermore, these early-time observations are likely probing synchrotron emission from particles accelerated during the initial flare or in a van der Laan (1966)-type phase, whereas our model captures the in situ particle acceleration powered by either the forward or reverse shock.

3.3 Fitting framework

We utilize nested sampling (Skilling 2004) package `dynesty`[3] (Speagle 2020) to ensure full exploration of posterior parameter space and to enable model comparison. We employ a standard Gaussian likelihood function:

$$\ln[L(\theta, \xi)] = -\frac{n}{2}\log(\sigma^2) - \frac{1}{2}\sum_{i=1}^{n}\left(\frac{x_i - \mu}{\sigma}\right)^2, \tag{3}$$

where x_n are the model fluxes and separations (which we jointly fit), μ and σ are the data and errors, respectively. For non-detections, we fit for a flux of 0 with errors consistent with the observed upper limits. We use 1024 live points, random walk sampling (`rwalk`), and the default multi-ellipsoidal decomposition (`multi`), which were found to provide a good balance between flexibility and computational cost. All fits were run with a consistent stopping criterion (`dlogz = 0.001`), where `dlogz` is the log of the ratio between the current estimated evidence and the remaining evidence. For all models, we present the natural logarithm of the Bayesian evidence (marginal likelihood) $\ln(Z)$ and the χ^2/dof values, where the degrees of freedom are the number of datapoints (79) less the number of free parameters.

3.4 Priors

In Table 1, we detail the prior constraints used for modelling. For the initial bulk Lorentz factor Γ_0 we use a log-uniform prior to ensure the model does not bias towards larger Lorentz factors unless required by the data. For the inclination angle, we adopt an isotropic (cosine[4]) prior, as expected from geometric arguments for an unknown value of $\theta_{\rm obs}$ (see discussion in Sections 2.1 and Appendix A). We do not include priors based on X-ray fits to disc emission/reflection due to the inconsistency between values derived from different models and the possibility of jet/disc misalignment. For the source distance, we adopt a prior based on the derived distance by Chauhan et al. (2019), with a normal distribution truncated at the authors' derived minimum and maximum distances, opting for a minimum distance of 3.5 kpc to account for the possibility of an association with an SNR located at this distance (Maxted et al. 2020). We opt to initially fit for magnetic energy fractions in the forward and reverse shocks individually, as GRB fits imply these values can differ ((Zhang, Kobayashi & Mészáros 2003; Harrison & Kobayashi 2013; Huang et al. 2016; Lamb et al. 2019; Lamb & Kobayashi 2019). These magnetic energy fractions $\epsilon_{\rm B}$ are chosen to have a large log-uniform range with a maximum at values corresponding to equipartition values e.g. $\epsilon_{\rm B,eq} = 0.5$.[5] For the surrounding ISM density we adopt a wide log-uniform prior to encompass very low densities predicted and inferred in cavities around X-ray binary jets (e.g. Hao & Zhang 2009; Carotenuto et al. 2024; Savard et al. 2025). We have three fixed parameters in the initial models, where the first two (the jet half-opening angle θ_c and the fractional energy transferred to electrons ϵ_e) are fixed to avoid degeneracies in posterior distributions. Around the launching time, Chauhan et al. (2021) were able to resolve the ejecta source size through long baseline radio observations and, by including observed proper motion, confidently identify the opening angle of the ejecta (independent of the angle to the line of sight). We fix this parameter to their best-fitting value of 4.5 deg. The fraction of energy in electrons is fixed to the maximum allowed value in equipartition of 0.5. We choose to adopt this maximum value for the initial models, such that our derived ejecta energy E_0 can be considered a minimum value: the energy in non-thermal particles is set by ϵ_e and the blastwave energy that depends on E_0. This means that generally, lower values of ϵ_e will result in a commensurately higher value of E_0.[6] Finally, the launch time of the ejecta is fixed based on kinematic-only constraints of Russell et al. (2019) and Carotenuto et al. (2024) and the radio/X-ray flaring activity observed at the time.[7]

4 RESULTS

4.1 Initial modelling

We initially fit four models, comprised of combinations of two jet profile morphologies (tophat & Gaussian) corresponding to uniform

---

[2] Future works, particularly where the ratio of separation to flux datapoints is larger or kinematic fits are unsatisfactory, may approximate systematic error using a percentage of the beam size where available.

[3] https://dynesty.readthedocs.io/en/stable/

[4] We note possible confusion between cosine/sin priors. This prior assumes isotropy that maximizes probabilities of jets at $\theta_{\rm obs} = 90$ deg and drops to zero at $\theta_{\rm obs} = 0$ deg.

[5] For a charge neutral electron–proton jet, the maximal equipartition value for $\epsilon_{\rm B}$ and ϵ_e would be 1/3, nevertheless we use 0.5 as a formal upper limit to conservatively account for the possibility of non-neutral or leptonic jets.

[6] Fixing the ϵ_e value has implications for the evolution of critical synchrotron frequencies. However, these frequencies are stable over the jet evolution (see Appendix B), meaning the result of variations in ϵ_e for these models is limited to the normalization of the flux. We verify this by testing additional models in which ϵ_e is allowed to vary freely (see Section 4.2).

[7] We note that the degeneracy in $\theta_{\rm obs}$ and β solution means that despite Carotenuto et al. (2024) finding a best-fit value of $\theta_{\rm obs} < 45$ deg, fixing the ejecta launch time to this date remains a reasonable choice (see Appendix A for more details).

Table 1. List of parameters for the initial models (A–D) with prior distributions and bounds. For later runs (A2–A6), the same free parameters and priors are used as here, unless explicitly stated in the text.

Parameter	Description	Prior	Bounds/value
Γ_0	Initial bulk Lorentz factor	Log-uniform	[1,10]
$E_{\rm iso,min}$	Isotropic-equivalent initial energy [erg]	Log-uniform	$[10^{40}, 10^{50}]$
$\theta_{\rm obs}$	Jet inclination angle (deg)	Cosine	[0,90]
D	Source distance (kpc)	Normal [Truncated]	$4.1^{+0.6}_{-0.6}$ [3.5, 6.7]
$n_{\rm ism}$	ISM (circumburst) density [cm^{-3}]	Log-uniform	$[10^{-8}, 1]$
$\epsilon_{\rm B,FS}$	Fraction of energy in forward shock magnetic field	Log-uniform	$[10^{-8}, 0.5]$
$\epsilon_{\rm B,RS}$	Fraction of energy in reverse shock magnetic field	Log-uniform	$[10^{-8}, 0.5]$
p	Power-law of accelerated electrons	Uniform	[2.2, 4.2]
$\theta_{\rm c}$	Half-opening angle of jet [deg]	**Fixed**	**2.25**
$\epsilon_{\rm e}$	Fraction of energy in accelerated electrons	**Fixed**	**0.5**
$t_{\rm ej}$	Launch time of ejecta	**Fixed**	**MJD 58017.4**

Table 2. Results of the initial modelling of four jet profiles, where tophat profile, non-spreading jet (Model A), performs best both in terms of the goodness of fit and Bayes factor.

Jet Model	Sub-type	log(Z)	Reduced χ^2	Bayes factor
Tophat	No Spreading (A)	$\mathbf{24.68 \pm 0.25}$	**1.57**	**1** (null)
	Spreading (B)	-10.89 ± 0.25	2.59	$\sim 10^{15}$
Gaussian	No Spreading (C)	19.27 ± 0.26	1.64	223
	Spreading (D)	-0.75 ± 0.26	2.20	$\sim 10^{11}$

and Gaussian-distributed jet energy (as defined by equations 59 and 60 in Wang et al. 2024), and turning lateral jet spreading on or off. These models are identical with the exception of jet morphology and spreading choices, and thus can be compared directly. Full details of these different jet models are available in Wang et al. (2024). In Table 2, we present the marginal likelihood, log(Z), and reduced Chi-squared, χ^2/dof, values for best-fitting parameter set obtained by each model. In each case, we also compute the Bayes Factor (ratio between marginal likelihoods) as compared to the best-performing Model (A). A Bayes factor of $\mathcal{B}$ can be interpreted as the null model (A) being a factor of $\mathcal{B}$ more likely as compared to the test model. Values of $\mathcal{B}$ greater than 100 imply decisive support for Model (A), the null hypothesis (Kass & Raftery 1995). We find conclusive evidence in favour of jets where spreading is turned off, as measured by both the reduced χ^2 and large Bayes factor values ($\mathcal{B}_{\rm BA} \gg 1$). The Bayes factor obtained comparing Model (C) to Model (A), $\mathcal{B}_{\rm CA} = 223$, implies weaker, yet still significant evidence that the data is best explained by a tophat rather than Gaussian profile jet.

In Fig. 1, we present the best-fitting Model (A) light-curve and kinematic fits, where in the top panel the total (forward + reverse shock) flux density is denoted by solid lines (coloured by frequency) and the forward shock component is highlighted as dashed lines. The corner plot is shown in Fig. 2. The reverse shock dominates initial emission before 100 d, with a sharp rise during the reverse shock crossing. After the reverse shock crosses, no new particles are accelerated and the flux declines sharply and $\nu_{\rm m}$ decreases. Shortly thereafter it decreases below $\nu_{\rm a}$ resulting in the emission fading more gradually, before the forward shock begins dominating emission. Both the reverse and forward shock emissions are optically thin and slow cooling throughout (e.g. the hierarchy $\nu_{\rm a} < \nu_{\rm obs} < \nu_{\rm c}$ holds throughout for both the reverse and forward shock at radio frequencies), with the exception of a short optically thick phase early in the evolution. This phase is very short (less than 10 d) for the preferred Model (A) and slightly longer for other models, but always shorter than the reverse shock crossing duration. This consistent hierarchy is expected based on the relatively stable observed spectral index of the jet ejecta (Russell et al. 2019), and means the evolution of light curves in all models (except the forward shock only Model A2) is driven primarily by the reverse shock crossing, the blastwave dynamical evolution, and the late-time brightening of the forward shock. Further discussion on the temporal evolution of the critical frequencies can be found in Appendix B. All four models tested follow similar profiles and best-fitting light curves and separation are presented in Appendix C.

In Table 3, we present the best-fitting values for the free parameters, quoting 1σ uncertainties assuming a Gaussian posterior distribution. Here, we briefly discuss the parameters, leaving most of the interpretation to Section 5. In all models, a relatively low initial Lorentz factor is derived, consistent with the lower range obtained by Carotenuto et al. (2024), with spreading jets requiring slightly higher values of Γ_0 and E_0 as expected. Consistently low ISM densities are derived and relatively high energies with minimum true (non-isotropic; $E_{\rm true} = E_{\rm iso}\theta_{\rm c}^2/4$) initial ejecta energies ranging from $E_{0,\rm min} = 3.4 - 5.9 \times 10^{43}$ erg. Taking the effective energy derived by kinematic-only modelling (Carotenuto et al. 2024) and substituting our derived Model (A) values of $n_{\rm ism}$ and fixed value of the half-opening angle, we find $E_{0,\rm C24} = 4.89^{+14.0}_{-3.37} \times 10^{43}$ erg, consistent with initial energies derived in this work. Our Model (A) initial energy and Lorentz factor imply a total initial ejecta mass of $M_0 = E_0/(\Gamma_0 - 1)c^2 = 1.1 \times 10^{23}$ g $\approx 5.5 \times 10^{-11}$ M$_\odot$.

In all models, the derived inclination angles are $\theta_{\rm obs} \sim 70$ deg, in agreement with the X-ray disc observations. The distance measurements are consistently pushed towards lowest value allowed in the prior of 3.5 kpc, which is also observed in the posterior distributions (see discussion in Section 5.6). Finally, the values of the electron power law p are relatively consistently placed around a reasonable value of 2.55, consistent with the observed spectral index of $\alpha \sim -0.75$ (where $F_\nu \propto \nu^\alpha$ and $p = 1 - 2\alpha$ for $\nu_{\rm obs} > \nu_{\rm m}$) in Russell et al. (2019). Surprisingly, the reverse shock magnetization, $\epsilon_{\rm B,RS}$, is very small, whereas typically in GRBs $\epsilon_{\rm B,RS} > \epsilon_{\rm B,FS}$. We run additional models in Section 4.2 to test this finding, and further discussion is continued in Section 5.

4.2 Further investigation

To interrogate our results, we test additional models with a variety of free parameter set-ups, using the best-fitting Model (A) scenario

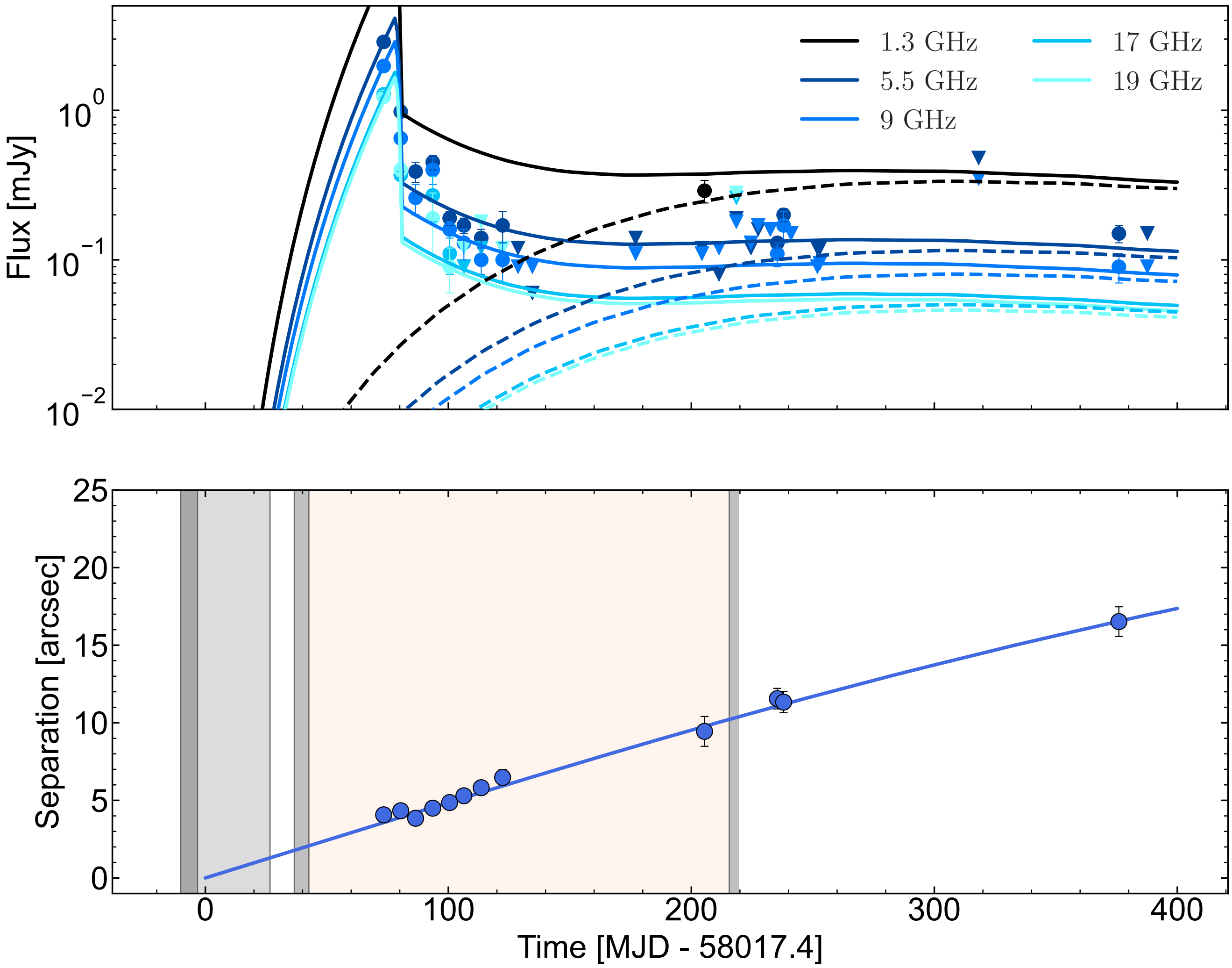

Figure 1. Preferred Model (A) light curves (top panel) and core-separation (bottom panel). In the top panel, the total flux density (reverse shock + forward shock) at observed frequencies is shown by the solid lines (lowest frequency = darkest, highest frequency = lightest), with the forward shock component denoted by dashed lines. Background shades in the bottom panel correspond to the X-ray state of MAXI J1535 from Tao et al. (2018): unshaded, darkest, medium, and lighest shades correspond to the hard, hard–intermediate, soft–intermediate, and soft states, respectively.

of a tophat jet without spreading. The results of these fits are shown in Table 4 with light curves and separations in Appendix C, and the parameter estimation for all models are shown in Table 5. We compute the reduced χ^2 and Bayes factor compared to Model (A) as before, but as model variations have varying numbers of free parameters, we also compute the Bayesian Information Criterion (BIC; Schwarz 1978):

$$\mathrm{BIC} = \kappa ln(n) - 2ln(L(\hat{\theta})), \tag{4}$$

where κ is the number of free parameters, $n = 79$ is the number of data points, and $ln(L(\hat{\theta}))$ is the log-likelihood of the parameters $\hat{\theta}$ that maximize the likelihood (e.g. best-fitting parameters). Lower relative values of BIC indicate preferred models and, unlike the Bayes factor, the BIC does not depend on the prior distribution.

4.2.1 *Single shock models*

In the first two (A2 and A3), we run Model (A) with only the forward shock (A2) and reverse shock (A3) contributing to emission. Both models perform poorly and are heavily disfavoured as compared to the combined Model (A), with the reverse shock only model performing better due to its ability to capture all early time data. Modification of our assumption of a uniform density ISM (e.g. without a cavity wall) may significantly improve the fit obtained by the forward shock only model, albeit with additional free parameters. None the less, we argue the reverse shock is necessary for the following reasons. First, the forward shock only Model (A2) requires unrealistic parameters, including $\Gamma_0 \gtrsim 10$ and $p \gtrsim 4.2$ (both posterior distributions bunch at the maximum prior value), where p especially is inconsistent with the observed spectral index. Crucially, the p value is pushed to unphysically high values merely to capture the steep decline in flux density, rather than matching the observed spectral index. Secondly, the forward shock only model predicts a very bright peak in emission prior to the first detection (see Fig. C2). However, the core flux detected at this time had a flat spectral index and occurred during a return to the X-ray hard state. This suggests the emission is consistent with compact jet emission, rather than early ejecta emission. Moreover, one of these significant core detections occurs on MJD 58 059 when the telescope is in a high spatial resolution configuration '6A', which should have resolved

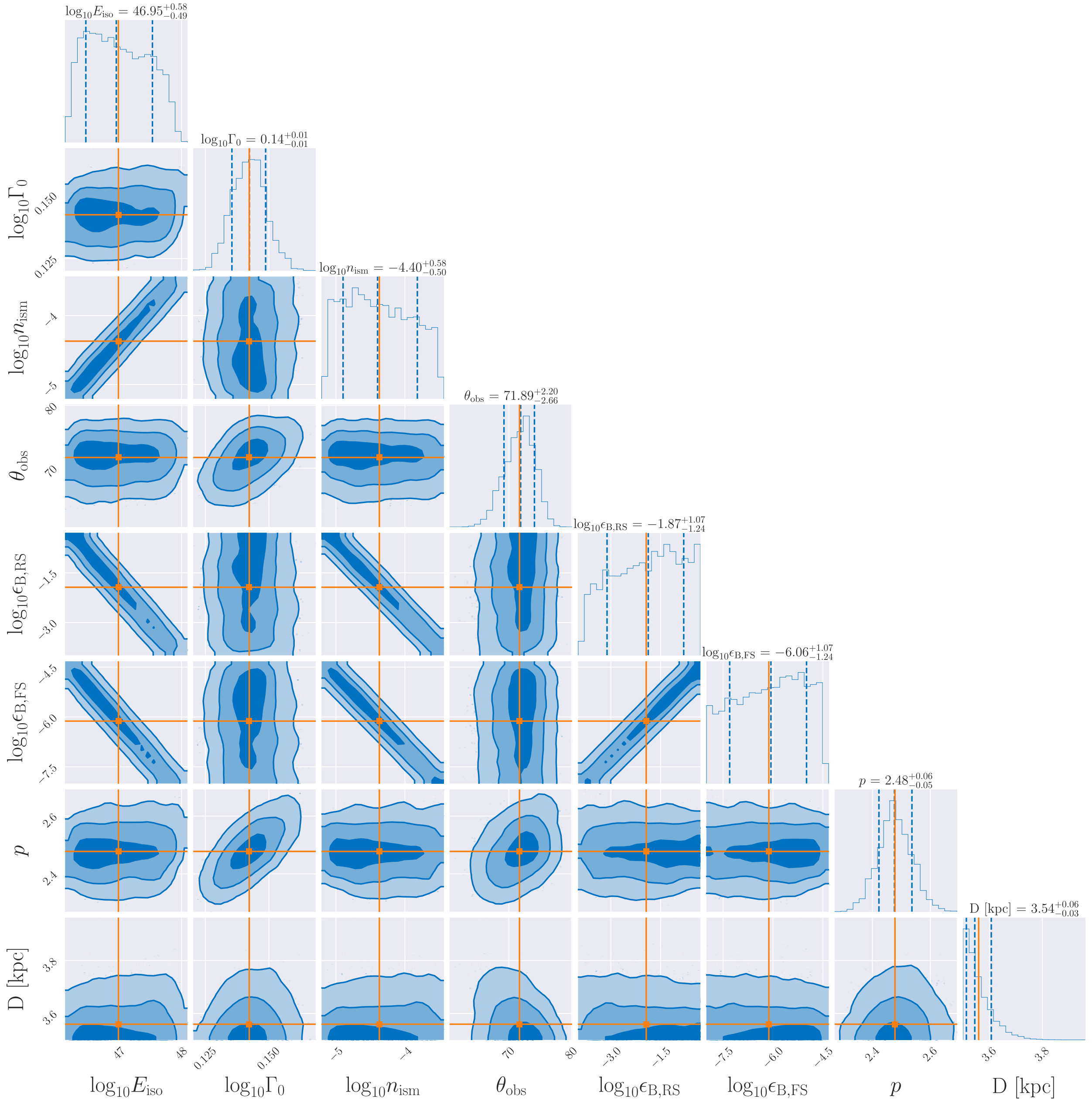

Figure 2. Corner plot of the posterior distributions for the best-fitting Model (A). The best-fitting value (mean of the posterior samples) is denoted in by solid lines, with the median and 1σ confidence interval (e.g. containing 68 per cent of posterior probability mass) with dashed lines. Only limited degeneracies are seen in key energetic parameters including $E_{\rm iso}$, $n_{\rm ism}$, and $\epsilon_{\rm B}$. The best-fitting distance is consistent with the minimum values of the prior constraint of 3.5 kpc.

Table 3. Parameter estimation for the initial models (A–D). We quote the median of the posterior distribution, with errors consistent with the 1σ confidence interval. Note that the minimum initial energy is the true (beaming-corrected) energy.

Jet Model	$\log_{10}E_{0,\rm min}$	Γ_0	$\log_{10}n_{\rm ism}$	$\theta_{\rm obs}$ [deg]	$\log_{10}\epsilon_{\rm B,RS}$	p	$\log_{10}\epsilon_{\rm B,FS}$	D [kpc]
Tophat no spread (A)	$43.54^{+0.58}_{-0.49}$	$1.38^{+0.02}_{-0.02}$	$-4.40^{+0.58}_{-0.50}$	$71.89^{+2.20}_{-2.66}$	$-6.06^{+1.07}_{-1.24}$	$2.48^{+0.06}_{-0.05}$	$-1.87^{+1.07}_{-1.24}$	$3.56^{+0.06}_{-0.03}$
Tophat spread (B)	$43.75^{+0.53}_{-0.53}$	$1.44^{+0.02}_{-0.02}$	$-4.34^{+0.54}_{-0.54}$	$79.41^{+1.98}_{-1.85}$	$-6.25^{+1.14}_{-1.16}$	$2.56^{+0.06}_{-0.06}$	$-1.95^{+1.14}_{-1.15}$	$3.52^{+0.02}_{-0.01}$
Gaussian no spread (C)	$43.53^{+0.59}_{-0.49}$	$1.41^{+0.02}_{-0.02}$	$-4.51^{+0.60}_{-0.48}$	$65.62^{+2.23}_{-2.32}$	$-5.82^{+1.03}_{-1.30}$	$2.53^{+0.05}_{-0.05}$	$-1.75^{+1.04}_{-1.28}$	$3.54^{+0.04}_{-0.02}$
Gaussian spread (D)	$43.77^{+0.60}_{-0.56}$	$1.46^{+0.02}_{-0.02}$	$-4.42^{+0.61}_{-0.56}$	$73.87^{+2.00}_{-2.12}$	$-6.13^{+1.19}_{-1.29}$	$2.60^{+0.05}_{-0.05}$	$-1.96^{+1.17}_{-1.30}$	$3.52^{+0.02}_{-0.01}$

Table 4. Results of the modelling of additional variations on the best-fitting Model (A), the details of which can be found in the discussion in Section 4.2.

Tophat no spread	Free Params	log(Z)	Reduced χ^2	BIC	Bayes Factor
(A) FS + RS base model	8	$\mathbf{24.68 \pm 0.25}$	1.57	**−77.96**	**1** (null)
(A2) FS only	7	-890.43 ± 0.22	27.13	1759.30	$\sim 10^{400}$
(A3) RS only	7	-69.55 ± 0.23	4.29	115.01	$\sim 10^{40}$
(A4) FS + RS (free ϵ_e[8])	9	22.80 ± 0.26	1.63	−71.09	6.5
(A5) FS + RS (free $\epsilon_{e,RS}$, $\epsilon_{e,FS}$, ϵ_B)	9	16.81 ± 0.28	**1.56**	−76.12	2618
(A6) FS + RS (free $\delta R_{RS}/\delta R_{FS}$)	9	24.43 ± 0.25	1.58	−74.57	1.28

[8] We relax the prior constraint in models where both ϵ_e and ϵ_B are fit to allow all values $\epsilon \leq 1$.

Table 5. Parameter estimation for Models (A) and (A4–A6) for energetically relevant parameters. Quoted values are the median of the posterior distribution, with errors consistent with the 1σ confidence interval. Note some models fit for a global $\epsilon_{B/e}$, whereas some fit independently for the forward and reverse shocks.

Jet model	$\log_{10}E_{\rm min}$	$\log_{10}n_{\rm ism}$	$\log_{10}\epsilon_{\rm B,(RS)}$	$\log_{10}\epsilon_{\rm B,FS}$	$\log_{10}\epsilon_{\rm e,(RS)}$	$\log_{10}\epsilon_{\rm e,FS}$	$\delta R_{\rm RS}/\delta R_{\rm FS}$
Model (A)	$43.54^{+0.58}_{-0.49}$	$-4.40^{+0.58}_{-0.50}$	$-6.06^{+1.07}_{-1.24}$	$-1.87^{+1.07}_{-1.24}$	0.5 (Fixed)	n/a	n/a
Model (A4) free ϵ_e	$43.90^{+0.46}_{-0.65}$	$-3.98^{+0.48}_{-0.66}$	$-5.55^{+1.02}_{-1.48}$	$-1.36^{+1.01}_{-1.49}$	$-0.92^{+0.63}_{-0.71}$	n/a	n/a
Model (A5) free $\epsilon_{e,RS}$, $\epsilon_{e,FS}$, ϵ_B	$43.10^{+0.31}_{-0.27}$	$-4.87^{+0.30}_{-0.26}$	$-0.20^{+0.14}_{-0.20}$	n/a	$-2.65^{+0.15}_{-0.20}$	$-0.88^{+0.61}_{-0.84}$	n/a
Model (A6) free $\delta R_{RS}/\delta R_{FS}$	$43.42^{+0.53}_{-0.37}$	$-4.59^{+0.55}_{-0.37}$	$-6.98^{+1.17}_{-0.73}$	$-1.48^{+0.80}_{-1.15}$	0.5 (Fixed)	n/a	$-0.71^{+0.52}_{-0.95}$

the ejecta. Finally, the model performs very poorly compared to reverse shock models even in explaining only early-time light curve and separation, implying multiple changes in density profile would be required to explain the data, including rebrightenings. Further discussion, including of the impact of a cavity wall on the reverse shock only model, is continued in Section 5.6.

4.2.2 Free global ϵ_e

In Model (A4), we include ϵ_e as an additional free parameter, and enforce a wider prior for ϵ_e as well as $\epsilon_{B,FS}$ and $\epsilon_{B,RS}$ to allow all values up to 1, no longer enforcing an equipartition maximum. This model performs well, yet the base model (A) with fixed ϵ_e is still marginally preferred by all metrics. This, in addition to the consistently high uncertainties in parameter estimation, implies that the data is not sufficient to support the inclusion of additional free parameters. In other words, a (limited) degeneracy is present between E_0, ϵ_e, and $n_{\rm ism}$ as hypothesized. Interestingly, despite magnetization parameters remaining consistent with Model (A), a lower value of $\epsilon_e \approx 0.1$, albeit with large uncertainties, is preferred. This change is commensurate with an increase in the initial energy ($E_{0,A4} \approx 8 \times 10^{43}$ erg), suggesting the initial energy should be slightly higher than our lower limit of $E_{0,A} \approx 4 \times 10^{43}$ erg found in Model (A).

4.2.3 Global ϵ_B, free ϵ_e

In Model (A5), we instead fit for a global ϵ_B which is applied to both the forward and reverse shock, and allow a freely varying ϵ_e parameter for each shock. This model is run to test the hypothesis whether the low derived value of $\epsilon_{B,RS}$ obtained in Model (A) merely reflects a lower particle acceleration or radiative efficiency (e.g. whether lower value of $\epsilon_{e,RS}$ can also reproduce the data). The model performs well, with the BIC and reduced χ^2 values very similar to Model (A), although the Bayes factor is disfavoured. The derived value of $\epsilon_{e,RS} \sim 10^{-2.7}$ and higher values of $\epsilon_{e,FS} \sim 10^{-0.9}$ and $\epsilon_B \sim 10^{-0.2}$ suggest we cannot draw any robust conclusions regarding the low inferred $\epsilon_{B,RS}$ from Model (A). In other words, we cannot distinguish the exact mechanism which limits the efficiency of the reverse shock emission with the present data, but merely that it is possibly due to low ϵ_e, ϵ_B, or both. The corner plot for this model is included in Appendix C.

4.2.4 Free reverse shock width

Finally, in Model (A6), we aim to test our underlying assumption that the shock thickness $\delta R_{FS} \sim \delta R_{RS}$. To do this, we again fix ϵ_e and fit for different ϵ_B values for each shock, but include a freely varying filling factor parameter $f = \delta R_{RS}/\delta R_{FS}$. This parameter is allowed to vary log-uniformly between $[10^{-6}, 1]$, where a value of 1 corresponds to the forward shock width computed by `jetsimpy`, e.g. Model (A). Variations in δR_{RS} in the model effectively result in commensurate changes the emissivity (as this calculated by dividing the rest-frame flux by the reverse shock volume) of the reverse shock without otherwise affecting the radiation calculations, unlike changes to ϵ_e. Across all metrics, Model (A6) performs well, but Model (A) is still marginally preferred.

The estimated filling factor is around $\delta R_{RS}/\delta R_{FS} \sim 0.19^{+0.45}_{-0.13}$ suggesting the base model is not vastly underestimating the volume of reverse shocked material, validating our methodology.

5 DISCUSSION

5.1 Initial energy and jet-launching mechanism

Our best-fitting initial energy, from Model (A), is $E_{0,\rm min} = 3.48^{+9.7}_{-2.36} \times 10^{43}$ erg, increasing to $E_0 = 7.90^{+15.01}_{-6.13} \times 10^{43}$ erg for Model (A4) where ϵ_e is allowed to vary freely, which may better reflect the true initial ejecta energy. We can compare these energy (and mass) estimates to the accretion flow properties over the jet-launching time-scale to attempt to discriminate between disc powered (Blandford & Payne 1982; BP82) and BH spin powered jets (Blandford & Znajek 1977; BZ77).

Self-absorbed radio flares are often observed around the launch of large-scale ejecta (Fender et al. 2009; Fender & Bright 2019), and their rise duration may correspond to the approximate launching time-scale of the ejecta such that $t_{\rm launch} \leq t_{\rm flare,rise}$. A bright radio flare was observed from MAXI J1535 around the launch of the ejecta component on MJD 58017. In addition, Chauhan et al. (2021) reported bright radio emission beginning to rise at 58017.17 and Russell et al. (2019) reported fading radio emission during a 3.5-h observation starting at MJD 58017.38. This implies a maximum flare rise time of approximately $t_{\mathrm{flare,rise}} \lesssim 5$ h and thus an ejection launch time less than 5 h. This is in agreement with discrete ejecta launching time-scales derived for MAXI J1820 + 070 through observations of quenching X-ray variability, Type B QPOs (Homan et al. 2020) and very long baseline imaging (Wood et al. 2021).

In the following, we compare the mass and energy budget of the ejecta to the disc properties across the launching time-scale. The estimated mass of the ejecta in our best-fitting Model (A) is 1.1×10^{23} g. The kinematically inferred launch time corresponds to a peak in the Swift/XRT X-ray light curve reported by Shang et al. (2019) on MJD 58017.03. The authors fit a two-component advective flow (TCAF; Chakrabarti & Titarchuk 1995) model and, assuming a fitted BH mass of $M_{\mathrm{BH}} = 8.1\,\mathrm{M}_{\odot}$, derive a mass accretion rate of $\dot{M}_{\mathrm{acc}} \approx 6.5 \times 10^{18}$ g s^{-1} where $\dot{M}_{\mathrm{acc}} = L_{\mathrm{acc}}/c^2$. We can compare this to MAXI observations presented by Sridhar et al. (2019), in which the authors reported $F_{\mathrm{bol}} = 1.6 \times 10^{-7}$ erg cm^{-2} s^{-1} on MJD 58007. Their fig. 1 shows that the MAXI flux doubled from MJD 58007–58017; therefore we estimate $F_{\mathrm{bol}} \approx 3 \times 10^{-7}$ erg cm^{-2} s^{-1} during the jet launching. Assuming $D \approx 4$ kpc, we estimate $L_{\mathrm{bol}} \approx 6 \times 10^{38}$ erg s^{-1}, and $\dot{M}_{\mathrm{accr}} \approx 6.4 \times 10^{18}$ g s^{-1}, approximately the same as Shang et al. (2019) for an accretion efficiency of 0.1.

Assuming the ejection duration of $\delta t_{\mathrm{launch}} = 5$ h, the mass accreted is 1.2×10^{23} g, only slightly larger than the ejecta mass. Under the assumption that the mass is accreted on to the BH (e.g. is not entrained in the jet), the total accretion required is $\dot{M}_{\mathrm{tot}} = \dot{M}_{\mathrm{ejecta}} + \dot{M}_{\mathrm{acc}} \approx 1.3 \times 10^{19}$ g s^{-1}. This requires an extremely efficient (50 per cent) mechanism of ejecting wind from the disc. We can compare this requirement with the $\dot{M}_{\mathrm{wind}}$ predicted by equation 5.2 of Blandford & Payne (1982). We assume that the magnetic field is in a magnetically arrested disc (MAD) state, given by the magnetic flux, $2\pi B R_{\mathrm{g}}^2$ and assume a maximally spinning BH ($a = 1$). Moreover, we set the logarithmic factor $\ln(R_{\mathrm{out}}/R_{\mathrm{in}}) = 1$ as the ejecta likely arises from the inner accretion flow, and neglect the difference between the poloidal and toroidal components of B (as they are similar in the BP82 model). In this case, $\dot{M}_{\mathrm{wind}} < (B R_{\mathrm{g}})^2/c$, where $B = \phi(\dot{M}_{\mathrm{acc}} c)^{1/2}/(2\pi R_{\mathrm{g}})$, and $\phi \approx 50$ for the most extreme case (Davis & Tchekhovskoy 2020). This gives $\dot{M}_{\mathrm{wind}} < (\phi/(2\pi))^2 \dot{M}_{\mathrm{acc}}$ which for our case gives $\dot{M}_{\mathrm{wind}} \lesssim 4 \times 10^{20}$ g s^{-1}. This is a naive estimate, based on X-ray model-dependent mass accretion rate estimates, but it shows that the BP82 disc wind model is capable of launching the wind required by our modelling if the mechanism is efficient.

The total ejection energy is $E \approx 3.5 \times 10^{43}$ erg. The required jet power over the 5 h launching duration is $L_{\mathrm{jet}} \approx 2 \times 10^{39}$ erg s^{-1}. This is consistent with the maximum possible MAD jet power (Davis & Tchekhovskoy 2020) for a BZ77 mechanism assuming a maximally spinning BH of $\dot{M}_{\mathrm{acc}} c^2 \approx 6 \times 10^{39}$ erg s^{-1}. However, the BZ77 mechanism predicts the jet is initially Poynting-flux dominated and only later can be loaded by mass (O' Riordan, Pe'er & McKinney 2018). Given the similarity of the derived values of $\dot{M}_{\mathrm{ejecta}}$ and $\dot{M}_{\mathrm{acc}}$, it remains a possibility that a large fraction of the accreted mass is entrained by a Blandford–Znajek jet.

5.2 Reverse shock

In this work, we have shown that while the forward shock is required for late-time emission, the reverse shock dominates bright, early emission from ejecta, in agreement with analytical estimates (Matthews et al. 2025) and relativistic hydrodynamic simulations (Savard et al. 2025). This is most easily demonstrated by how poorly the forward-shock-only Model (A3) performs (see Section 4.2), primarily due to the steep decline of the early light curve. This finding is in agreement with conclusions of previous work (Wang et al. 2003; Hao & Zhang 2009), where it was concluded that a forward shock would evolve too slowly to explain the observed light-curve evolution for the ejecta from XTE J1550−564.

5.2.1 *Crossing time-scale*

Generically, the reverse shock crossing time is pinpointed by the first peak of emission. In our best-fitting light curves, all models typically infer a reverse shock crossing time slightly later than the first datapoint (MJD 58090.78), which was the brightest observed. This sharp rise during the reverse shock crossing explains why the ejecta was not detected on MJD 58 059 and MJD 58080, where ATCA observations were taken with a sufficiently high angular resolution (the beamsize along the jet axis was around 1 arcsec in both observations) to spatially resolve the ejecta from the core (see further discussion in Russell et al. 2019, Section 3.4). None the less, earlier time observations, particularly covering the reverse shock crossing at lower frequencies, could be invaluable for future modelling. This is especially important in determining the initial Lorentz factor, ejecta energy, and ISM density which are the primary parameters setting the reverse shock crossing time-scale.

The peak of the reverse shock emission coincides temporally with a significant sudden reduction in the ejecta separation measurement ~90 d post launch. As the reverse shock crosses the ejecta, material at the front will radiate and cool before material at the back, resulting in the best-fitting centroid may appear to slow or possible reverse direction. Furthermore, the transition between reverse and forward shock dominated emission zones may result in the opposite effect. Higher angular resolution observations around this crucial phase, (assuming emission is not resolved out), will help elucidate whether additional information regarding the blastwave geometry can be obtained through the observations of the reverse-forward shock transition. Full interpretation of such observations will require improved modelling through distinct modelling of the core-separation of reverse and forward shocked material, or synthetic radio images of ejecta simulations (Wang et al. 2024; Savard et al. 2025).

5.2.2 *Efficiency*

Our best-fitting Model (A) implies an unexpectedly low magnetization for the reverse shocked material, in stark contrast with GRB models which typically require $\epsilon_{\mathrm{B,RS}} > \epsilon_{\mathrm{B,FS}}$. The results of Model (A6) imply our underlying assumption of the geometry of the reverse shock is approximately correct and cannot explain the low magnetization as a model-dependent effect. It is plausible this result may reflect a fundamental difference between reverse shocks in violent GRBs and relatively mild accretion energetics of XRB ejecta. However, further testing, especially the satisfactory fit to the data obtained by Model (A5), suggests that our finding could be merely a manifestation of a low value of $\epsilon_{\mathrm{e,RS}}$ (the fraction of energy transferred to the acceleration of electrons). We conclude that the reverse shock is likely characterized by either low magnetization or low particle acceleration efficiency, which may be tested by future modelling of other BH-XRB sources.

5.3 Underdense interstellar medium

In all models, we ubiquitously find interstellar media densities much lower than the canonical ISM density of $n \sim 1\mathrm{cm}^{-3}$. This finding supports the long-standing hypothesis that the environment of XRBs, at least along the jet axis of sources which produce discrete ejecta, are characterized by an underdense media (Heinz 2002; Carotenuto et al. 2024). Moreover, there is evidence that the most powerful, furthest propagating ejecta may reach the edge of such a cavity (Hao & Zhang 2009; Carotenuto et al. 2022; Zdziarski et al. 2023). Such cavities are suggested to have formed due to previous jet activity (Gallo et al. 2005; Carotenuto et al. 2022; Sikora & Zdziarski 2023; Savard et al. 2025). There is tentative evidence that the supernova remnant (SNR) G323.7−1.0 was associated with the formation of MAXI J1535 and may have resulted in the underdense cavity (Maxted et al. 2020). The cavity's observed distance of 3.5 kpc and spatial size of tens of arcminutes appear to agree with our distance estimate and our assumption that ejecta-cavity interaction is not significant for this source. However, XRBs with low mass companions are generally expected to be relatively old (100s Myr), such that the SNR associated with BH formation is no longer observable; therefore, further evidence is required for a robust association.

5.4 Jet profile and spreading

Our model comparison shows clear evidence that the MAXI J1535 data is best fit by a jet which does not undergo significant lateral spreading. Inspection of best-fitting kinematics plots (see Appendix C) imply the late-time data, particularly the final datapoints on MJD 58393, are consistently under predicted by models where spreading is enabled. Lateral jet spreading likely occurs due to transverse motion induced by internal pressure gradients acting on the surrounding media, and therefore is expected to become significant only after a reverse shock heats jet material. However, the reverse shock crossing time represents a much larger fraction of the overall evolution for XRB jets than GRBs (Matthews et al. 2025), owing in part due to the low sound speed $c_s \ll \beta_{\rm jet}$. For this reason, jet spreading is possibly much less significant for mildly relativistic blast waves, including XRBs ejecta. Our findings also show significant, albeit less decisive, preference for tophat jets over Gaussian profile jets, although given the lower Bayes factor $\mathcal{B} = 223$, further evidence is required to confirm this.

5.5 Inclination angle

All models find a large jet viewing angle of $\theta_{\rm obs} = 65 - 80$ deg in good agreement with the consensus from X-ray disc reflection features. This suggests that jet axis and the disc face are likely perpendicularly aligned.

Our finding of a larger $\theta_{\rm obs}$ than previous works implies an initial Doppler factor for the approaching jet (assuming $\Gamma \lesssim 1.4$ and $\theta_{\rm obs} \gtrsim 60$ degrees) of $\delta_{\rm app} \lesssim 1.1$ and $\delta_{\rm rec} \gtrsim 0.5$. We can crudely estimate the peak receding flux density, taking into account our derived spectral index of $\alpha \approx 0.75$, using the fact that $f_{\rm rec} \approx f_{\rm app}\delta_{\rm rec}^{3-\alpha}/\delta_{\rm app}^{3-\alpha}$. The peak observed flux density of $f_{\rm app} = 2.87$ mJy corresponds to an estimated receding jet flux of $f_{\rm rec} \gtrsim 0.15$ mJy, depending on the deceleration profile and real value of $\theta_{\rm obs}$. In the case of MAXI J1535, no receding jet was detected in the observations. Such a detection may be confounded by the receding jet having a smaller core-separation, greatly exacerbated by the poor angular resolution of early ATCA observations (Russell et al. 2019), and thus the receding ejecta component may be difficult to distinguish from core emission which remained bright until MJD 58150. Future modelling may be improved by incorporating non-detections of receding jets, particularly with high resolution instrumentation, to further constrain the jet inclination angle and initial Lorentz factor. A detailed discussion on observing receding jets will be presented in a future work.

5.6 Caveats

There are a number of caveats to this work related to the limitations of the model. The first major caveat is our assumption that the reverse shock is co-spatial with the forward shock in volume and core-separation. This is required in the model such that an emissivity can be calculated in the `jetsimpy` custom radiation model and is generally motivated by the fact that the outflow width is much less than the ejecta propagation distance. Nevertheless, we interrogate this assumption in our Model (A6), where the shock width (and effectively, the volume of reverse-shocked material) is a free parameter, and find this likely plays a minor role.

In the core-separation modelling, we use the `jet.Offset` function in `jetsimpy`, which strictly tracks only the core separation of the forward shock emission region. However, this is a valid approximation during and shortly after the reverse shock crossing, as the forward and reverse shocks have very similar core-separations (see fig. 9 in Matthews et al. 2025). Crucially, this is precisely when we expect the reverse shock emission to dominate over the forward shock, and thus we do not expect this to significantly affect our results. However, an exciting prospect is that future high-resolution observations could observe distinct components corresponding to the forward and reverse shock, particularly in the time-frame directly after the crossing, where both shocks significantly contribute to emission.

Another caveat to this work is the assumed uniform density profile of the ISM. Carotenuto et al. (2022) found that a two-stage cavity/ISM media best fit the kinematic data of MAXI J1348−630. Additional deceleration upon jet–cavity interaction may result in late-time rebrightenings as observed from MAXI J1535 around 380 d post-launch. Although our findings clearly require reverse shock emission due to the lack of resolved jet ejecta before 85 d post-burst and the sharp decay of the light curve (see discussion in Section 4.2, also Wang et al. 2003), we consider it conceivable, but very unlikely, that the reverse shocked material could persist to produce observed late-time emission due to jet–ISM interactions. This is disfavoured, as late-time rebrightenings likely require *in situ* particle acceleration (Bright et al. 2020), which does not occur within the actual ejecta material after the reverse shock has already crossed. Furthermore, core separation of reverse-shocked material slows drastically at late times (Matthews et al. 2025), making it difficult to reach observed late-time separation. None the less, future joint radiative and kinematic modelling may include models containing a cavity via changes to the ISM density profile to verify our conclusion that both shocks are required to explain the data. Finally, a simple way to verify the presence of forward shock emission at late times would be to conduct a single deep observation at late times, after non-detection in shorter integration time observations. Jet–cavity interactions of reverse-shocked material would fade much faster than a forward shock, which evolves on longer time-scales.

The final caveat to this work is that the derived distance is found to be at the lowest end of the prior distribution in all models. The prior is enforced based on independent and robust observational constraints obtained by Chauhan et al. (2019) and therefore is likely representative of a systematic in the model. If indeed MAXI J1535 is located at a distance closer than 3.5 kpc, the observed luminosity and core–jet separation will increase, and therefore will result in a lower value of E_0 (and commensurately higher value of $n_{\rm ism}$).

6 CONCLUSIONS AND OUTLOOK

In this work, we have performed joint radiative and kinematic modelling of XRB ejecta from MAXI J1535. We successfully fit both the flux and kinematic data from this source, demonstrating how combining flux and separation data for these sources allows us to break key energetic degeneracies, significantly improving parameter estimation. Our primary conclusions are as follows:

(i) The reverse shock dominates the MAXI J1535 ejecta emission at early times and is characterized by either low magnetization or inefficient particle acceleration.

(ii) The jet has a moderate initial Lorentz factor $\Gamma \approx 1.4$, does not undergo significant lateral spreading, and is likely launched perpendicular to the disc.

(iii) The initial ejecta energy is $E_0 \gtrsim$ few $\times\ 10^{43}$ erg and may be powered by the accretion disc alone.

(iv) The ejecta propagates into a low $n_{\rm ism} < 10^{-4}$ cm^{-3} density environment.

These findings are in good agreement with previous work (Wang et al. 2003; Carotenuto et al. 2024) and motivate future theoretical and observational investigation. Modelling of additional XRB ejecta sources with sufficient temporal and frequency coverage will be essential to ascertain whether the findings of this work apply ubiquitously. Sources with early-time observations covering the rise corresponding to the reverse shock crossing, those with high luminosities that may be incompatible with disc-powered jets, and sources where receding jets are also detected represent the most interesting sources to which similar modelling could be applied. Future work would benefit from the development of dedicated blast-wave models that produce kinematic and radiative predictions for trans-relativistic, off-axis jets that explicitly include the reverse shock. This could be realized through the development of an MHD simulation grid from which radiation and kinematic predictions could be fit to the data by interpolating between models. Crucially, such an approach could take advantage of kinematic degeneracies (e.g. between E_0 and $n_{\rm ism}$) to reduce the total number of runs required to cover the parameter space. Finally, polarization measurements throughout the ejecta evolution may represent an additional dimension for modelling, if robust theoretical predictions can be folded into the model.

ACKNOWLEDGEMENTS

The authors would like to thank the anonymous referee for useful comments that improved this manuscript. AJC thanks H. Wang for the publication of, and advice in using, `jetsimpy`, and H. Gao for useful insights regarding reverse shock models. AJC also acknowledges fruitful discussions with D. Aksulu, A. van der Horst, A. Hughes, and the XKAT Collaboration.

AJC acknowledges support from the Oxford Hintze Centre for Astrophysical Surveys which is funded through generous support from the Hintze Family Charitable Foundation. JHM acknowledges funding from a Royal Society University Research Fellowship (URF\R1\221062). RF acknowledges support from UK Research and Innovation, The European Research Council, and the Hintze Family Charitable Foundation. GPL was supported by a Royal Society Dorothy Hodgkin Fellowship (grant nos. DHF-R1-221175 and DHF-ERE-221005). TDR acknowledges support as an INAF IAF research fellow. NS acknowledges support from the Knut and Alice Wallenberg Foundation through the ‘Gravity Meets Light’ project and by the research environment grant ‘Gravitational Radiation and Electromagnetic Astrophysical Transients’ (GREAT) funded by the Swedish Research Council (VR) under Dnr 2016–06012. KS acknowledges support from the Clarendon Scholarship Program at the University of Oxford and the Lester B. Pearson Studentship at St John’s College, Oxford. AAZ acknowledges support from the Polish National Science Center grants 2019/35/B/ST9/03944 and 2023/48/Q/ST9/00138.

DATA AVAILABILITY

All observational data presented in this work are freely available in the referenced material, but will also be provided upon request to the authors. A full reproduction package, including theoretical models, data products, and plots will be made available at: https://github.com/alexanderjsc after publication.

REFERENCES

Abeysekara A. U. et al., 2018, Nature, 562, 82
Aharonian F. et al., 2005, Science, 309, 746
Albert J. et al., 2006, Science, 312, 1771
Albert J. et al., 2007, ApJ, 665, L51
Arnaud K. A., 1996, in Jacoby G. H., Barnes J., eds, ASP Conf. Ser. Vol. 101, Astronomical Data Analysis Software and Systems V. Astron. Soc. Pac., San Francisco, p. 17
Bahramian A. et al., 2023, ApJ, 948, L7
Blandford R. D., McKee C. F., 1976, Phys. Fluids, 19, 1130
Blandford R. D., Payne D. G., 1982, MNRAS, 199, 883
Blandford R. D., Znajek R. L., 1977, MNRAS, 179, 433
Blandford R., Meier D., Readhead A., 2019, ARA&A, 57, 467
Bright J. S. et al., 2020, Nat. Astron., 4, 697
Carotenuto F. et al., 2021, MNRAS, 504, 444
Carotenuto F., Tetarenko A. J., Corbel S., 2022, MNRAS, 511, 4826
Carotenuto F., Fender R., Tetarenko A. J., Corbel S., Zdziarski A. A., Shaik G., Cooper A. J., Di Palma I., 2024, MNRAS, 533, 4188
Chakrabarti S., Titarchuk L. G., 1995, ApJ, 455, 623
Chauhan J. et al., 2019, MNRAS, 488, L129
Chauhan J. et al., 2021, PASA, 38, e045
Cooper A. J., Gaggero D., Markoff S., Zhang S., 2020, MNRAS, 493, 3212
Corbel S., Fender R. P., Tzioumis A. K., Tomsick J. A., Orosz J. A., Miller J. M., Wijnands R., Kaaret P., 2002, Science, 298, 196
Corbel S., Kaaret P., Fender R. P., Tzioumis A. K., Tomsick J. A., Orosz J. A., 2005, ApJ, 632, 504
Davis S. W., Tchekhovskoy A., 2020, ARA&A, 58, 407
Dincer T., 2017, Astron. Telegram, 10716, 1
Dong Y., Liu Z., Tuo Y., Steiner J. F., Ge M., García J. A., Cao X., 2022, MNRAS, 514, 1422
Fender R., Bright J., 2019, MNRAS, 489, 4836
Fender R. P., Belloni T. M., Gallo E., 2004, MNRAS, 355, 1105
Fender R. P., Maccarone T. J., van Kesteren Z., 2005, MNRAS, 360, 1085
Fender R. P., Homan J., Belloni T. M., 2009, MNRAS, 396, 1370
Fender R. et al., 2016, in MeerKAT Science: On the Pathway to the SKA. Procedings of Science, Trieste, p. 13
Ferrarese L., Merritt D., 2000, ApJ, 539, L9
Gallo E., Corbel S., Fender R. P., Maccarone T. J., Tzioumis A. K., 2004, MNRAS, 347, L52
Gallo E., Fender R., Kaiser C., Russell D., Morganti R., Oosterloo T., Heinz S., 2005, Nature, 436, 819
Gao H., Lei W.-H., Zou Y.-C., Wu X.-F., Zhang B., 2013, New Astron. Rev., 57, 141
Gehrels N. et al., 2004, ApJ, 611, 1005

Hannikainen D., Campbell-Wilson D., Hunstead R., McIntyre V., Lovell J., Reynolds J., Tzioumis T., Wu K., 2001, Astrophys. Space Sci. Supp., 276, 45

Hao J. F., Zhang S. N., 2009, ApJ, 702, 1648

Harrison R., Kobayashi S., 2013, ApJ, 772, 101

Heinz S., 2002, A&A, 388, L40

Heinz S., Sunyaev R., 2002, A&A, 390, 751

Heinz S., Merloni A., Schwab J., 2007, ApJ, 658, L9

Heinz S., Grimm H. J., Sunyaev R. A., Fender R. P., 2008, ApJ, 686, 1145

Hjellming R. M. et al., 2000, ApJ, 544, 977

Homan J. et al., 2020, ApJ, 891, L29

Huang Y. F., Dai Z. G., Lu T., 1999, MNRAS, 309, 513

Huang X.-L., Xin L.-P., Yi S.-X., Zhong S.-Q., Qiu Y.-L., Deng J.-S., Wei J.-Y., Liang E.-W., 2016, ApJ, 833, 100

Huang Y. et al., 2018, ApJ, 866, 122

Ingram A. R., Motta S. E., 2019, New Astron. Rev., 85, 101524

Kantzas D., Markoff S., Cooper A. J., Gaggero D., Petropoulou M., De La Torre Luque P., 2023, MNRAS, 524, 1326

Kass R. E., Raftery A. E., 1995, J. Am. Stat. Assoc., 90, 773

Kimura S. S., Sudoh T., Kashiyama K., Kawanaka N., 2021, ApJ, 915, 31

Kobayashi S., 2000, ApJ, 545, 807

Kuze R., Kimura S. S., Fang K., 2025, ApJ, 985, 139

LHAASO Collaboration, 2024, preprint (arXiv:2410.08988)

Lamb G. P., Kobayashi S., 2019, MNRAS, 489, 1820

Lamb G. P. et al., 2019, ApJ, 883, 48

Lasota J.-P., 2001, New Astron. Rev., 45, 449

Matsuoka M. et al., 2009, PASJ, 61, 999

Matthews J. H. et al., 2025, MNRAS, 539, 2665

Maxted N. I., Ruiter A. J., Belczynski K., Seitenzahl I. R., Crocker R. M., 2020, preprint (arXiv:2010.15341)

Miller-Jones J. C. A. et al., 2019, Nature, 569, 374

Miller J. M. et al., 2018, ApJ, 860, L28

Mioduszewski A. J., Rupen M. P., Hjellming R. M., Pooley G. G., Waltman E. B., 2001, ApJ, 553, 766

Mirabel I. F., Rodríguez L. F., 1994, Nature, 371, 46

Motta S. E., 2016, Astron. Nachr., 337, 398

Nakahira S. et al., 2018, PASJ, 70, 95

Negoro H. et al., 2017, Astro. Telegram, 10699, 1

O' Riordan M., Pe'er A., McKinney J. C., 2018, ApJ, 853, 44

Parikh A. S., Russell T. D., Wijnands R., Miller-Jones J. C. A., Sivakoff G. R., Tetarenko A. J., 2019, ApJ, 878, L28

Rees M. J., 1966, Nature, 211, 468

Remillard R. A., McClintock J. E., 2006, ARA&A, 44, 49

Rushton A. P. et al., 2017, MNRAS, 468, 2788

Russell T. D., Soria R., Miller-Jones J. C. A., Curran P. A., Markoff S., Russell D. M., Sivakoff G. R., 2014, MNRAS, 439, 1390

Russell T. D., Miller-Jones J. C. A., Sivakoff G. R., Tetarenko A. J., Jacpot Xrb Collaboration, 2017, Astron. Telegram, 10711, 1

Russell T. D. et al., 2019, ApJ, 883, 198

Russell T. D. et al., 2020, MNRAS, 498, 5772

Ryan G., van Eerten H., Troja E., Piro L., O'Connor B., Ricci R., 2024, ApJ, 975, 131

Sarath A., Böttcher M., 2025, ApJ, 984, 168

Savard K., Matthews J. H., Fender R., Heywood I., 2025, MNRAS, 540, 1084

Schwarz G., 1978, Ann. Stat., 6, 461

Sedov L. I., 1959, Similarity and Dimensional Methods in Mechanics. CRC Press, Boca Raton

Shang J. R., Debnath D., Chatterjee D., Jana A., Chakrabarti S. K., Chang H. K., Yap Y. X., Chiu C. L., 2019, ApJ, 875, 4

Sikora M., Zdziarski A. A., 2023, ApJ, 954, L30

Sironi L., Giannios D., 2013, ApJ, 778, 107

Skilling J., 2004, in Fischer R., Preuss R., Toussaint U. V., eds, AIP Conf. Ser. Vol. 735, Bayesian Inference and Maximum Entropy Methods in Science and Engineering: 24th International Workshop on Bayesian Inference and Maximum Entropy Methods in Science and Engineering. Am. Inst. Phys., New York, p. 395

Speagle J. S., 2020, MNRAS, 493, 3132

Sreehari H., Ravishankar B. T., Iyer N., Agrawal V. K., Katoch T. B., Mandal S., Nandi A., 2019, MNRAS, 487, 928

Sridhar N., Bhattacharyya S., Chandra S., Antia H. M., 2019, MNRAS, 487, 4221

Steiner J. F., McClintock J. E., 2012, ApJ, 745, 136

Steiner J. F., McClintock J. E., Reid M. J., 2012, ApJ, 745, L7

Stevens A. L. et al., 2018, ApJ, 865, L15

Tao L. et al., 2018, MNRAS, 480, 4443

van der Laan H., 1966, Nature, 211, 1131

Vincentelli F. M. et al., 2021, MNRAS, 503, 614

Wang X. Y., Dai Z. G., Lu T., 2003, ApJ, 592, 347

Wang H., Dastidar R. G., Giannios D., Duffell P. C., 2024, ApJS, 273, 17

Williams D. R. A. et al., 2022, MNRAS, 517, 2801

Wood C. M. et al., 2021, MNRAS, 505, 3393

Wood C. M. et al., 2023, MNRAS, 522, 70

Xu Y. et al., 2018, ApJ, 852, L34

Yang J., Brocksopp C., Corbel S., Paragi Z., Tzioumis T., Fender R. P., 2010, MNRAS, 409, L64

Zdziarski A. A., Sikora M., Szanecki M., Böttcher M., 2023, ApJ, 947, L32

Zdziarski A. A., Wood C. M., Carotenuto F., 2025, ApJ, 986, L35

Zhang B., Kobayashi S., Mészáros P., 2003, ApJ, 595, 950

Zhang X. et al., 2025, preprint (arXiv:2504.11945)

APPENDIX A: CONSTRAINING THE JET INCLINATION ANGLE FOR A GIVEN PROPER MOTION

As discussed in Section 2.1, we re-examined constraints on the jet angle to the line of sight ($\theta_{\rm obs}$) presented in Russell et al. (2019), and found additional solutions which allowed a larger range of $\theta_{\rm obs}$. In Fig. A1, we present our new $\theta_{\rm obs}$–β solutions, recreating fig. 9 of Russell et al. (2019).

The new solutions exist above an inflection point, representing an upper branch for which similar values of β can result in larger inclination angles. Generically, one can derive a threshold value of proper motion as a function of source distance of 173.5 mas day^{-1} kpc^{-1}, above which the inclination angle can be constrained to $\theta_{\rm obs} < 90$ deg (see also Zdziarski, Wood & Carotenuto 2025). This is equivalent to the condition for apparent superluminal motion. We include the updated constraints for the assumed distances in Table A1 and also update the inclination angle constraints for MAXI J1348−630 from Carotenuto et al. (2021) for which similar extension to the published solutions exists. Finally, we note that in the kinematic-only modelling of Carotenuto et al. (2024), the authors

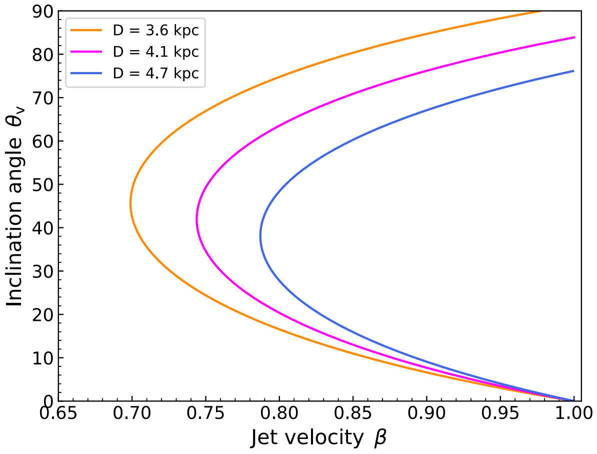

Figure A1. Updated inclination angle as a function of jet velocity $\beta = v/c$ for the maximum observer proper motion from MAXI J1535 of 47 mas d^{-1}.

Table A1. Updated jet angle to the observer line of sight proper motion upper limit constraints assuming the maximum best-fitting proper motion values of 47 mas d^{-1} (MAXI J1535−571; Russell et al. 2019) and 108 mas d^{-1} (MAXI J1348−630; Carotenuto et al. 2021).

Source	Distance [kpc]	Constraint [deg]
MAXI J1535-571	3.6	n/a
	4.1	83.3
	4.6	75.6
MAXI J1348-630	1.6	89.6
	2.2	71.4
	2.7	60.5

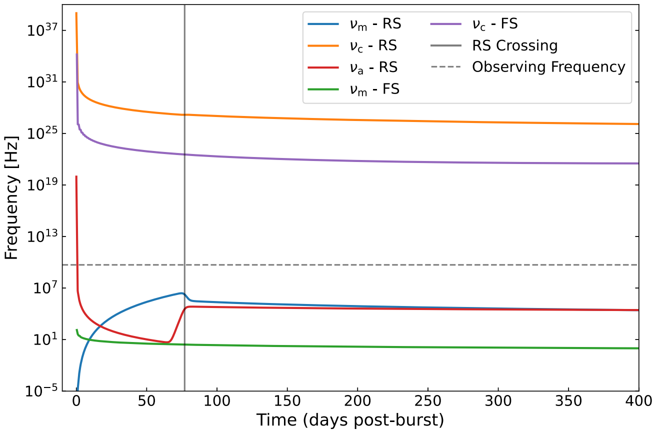

Figure B1. Evolution of the peak, self-absorption, and cooling synchrotron frequencies for the preferred Model (A). The critical frequencies are averaged in 800 s bins to account for different values at different regions in the hydrodynamic shock front, and for the reverse shock interpolated across the shock crossing time for readability.

best-fitting inclination angle $\theta_{\rm obs} = 30.3 \pm 6.3$ deg is much lower than the typical values in this work. However, this is not in tension as it appears, due to the degeneracy about a critical inflection point in Fig. A1. The derived value of β is similar for both models, as would be expected given the similar kinematic profile.

APPENDIX B: HIERARCHY OF CRITICAL FREQUENCIES

In order to model the light curve of the ejecta using `jetsimpy`, the critical synchrotron frequencies (absorption $\nu_{\rm a}$, minimum/peak $\nu_{\rm m}$, and cooling $\nu_{\rm c}$) are computed separately for the forward and reverse shock as a function of the time-dependent blastwave properties. For the forward shock we use the standard `sync_dn` model in `jetsimpy` (Wang et al. 2024), and for the reverse shock we employ the prescription developed by Kobayashi (2000) as presented in Gao et al. (2013). In Fig. B1, we show the evolution of all relevant critical frequencies as a function of observer-frame time for the preferred Model (A). The forward shock model in `jetsimpy` does not account for synchrotron self-absorption, so $\nu_{\rm a,FS}$ is not included in the plot. However in all models the forward shock is not relevant until late-times, where it is characterized by lower flux densities and larger spatial scales than the reverse shock, meaning that we can safely assume that $\nu_{\rm a,FS} < \nu_{\rm a,RS} < \nu_{\rm obs}$.

APPENDIX C: ADDITIONAL PLOTS

All best-fitting light curve and kinematic plots from all tested models will be made available online after publication. In this Appendix, we include a few useful diagnostic plots. In Fig. C1, we show a random sample of 30 light curves and separations from Model (A) obtained from the posterior parameter distribution to give an indication of model uncertainties. For clarity, fluxes and upper limits in the top panel are scaled to a common frequency of 5.5 GHz. The reverse shock crossing time is pinpointed by the available data, but some discrepancies are observed in the posterior distribution at late-times, likely owing to the lack of data and the uncertainties associated with faint detections.

In Fig. C2, we show the best-fitting light curves and separations for all models. With the notable exception of the FS-only (A3) and RS-only (A2) models, all follow similar light-curve patterns with the reverse shock peaking at the crossing time at 90 d post-burst, and a late-time rebrightening powered by the forward shock. The forward shock only Model (A3) predicts a very bright early light curve, fails to explain late-time detections, and does not propagate to the required separation and late-times as discussed in Section 4.2. The reverse shock only model does much better, but also fails to capture the late-time re-brightening. In general, the two spreading jet models (B) and (D) struggle to reproduce the final datapoints for both the light-curve and kinematic profiles. All other models (A, A4, A5, A6, and C) are non-spreading jets with different free parameters setting microphysical radiation are somewhat comparable. Finally, we note the light curve for Model (A5) is plotted from 60 d and onwards as it is (exceptionally) self-absorbed until this time, likely due to the much larger $\epsilon_{\rm B}$, for which the flux is not well-defined in the model.

Finally, in Fig. C3 we show the corner plot for Model (A5), which produces the best χ^2 value and the second best BIC score. This model finds relatively high value for $\epsilon_{\rm B} \sim 0.1$, but a much lower value for $\epsilon_{\rm e,RS} \sim 10^{-2.65}$, meaning we cannot conclude the reverse shock has low magnetization, as the data is almost equally well explained by a low value of $\epsilon_{\rm e,RS}$.

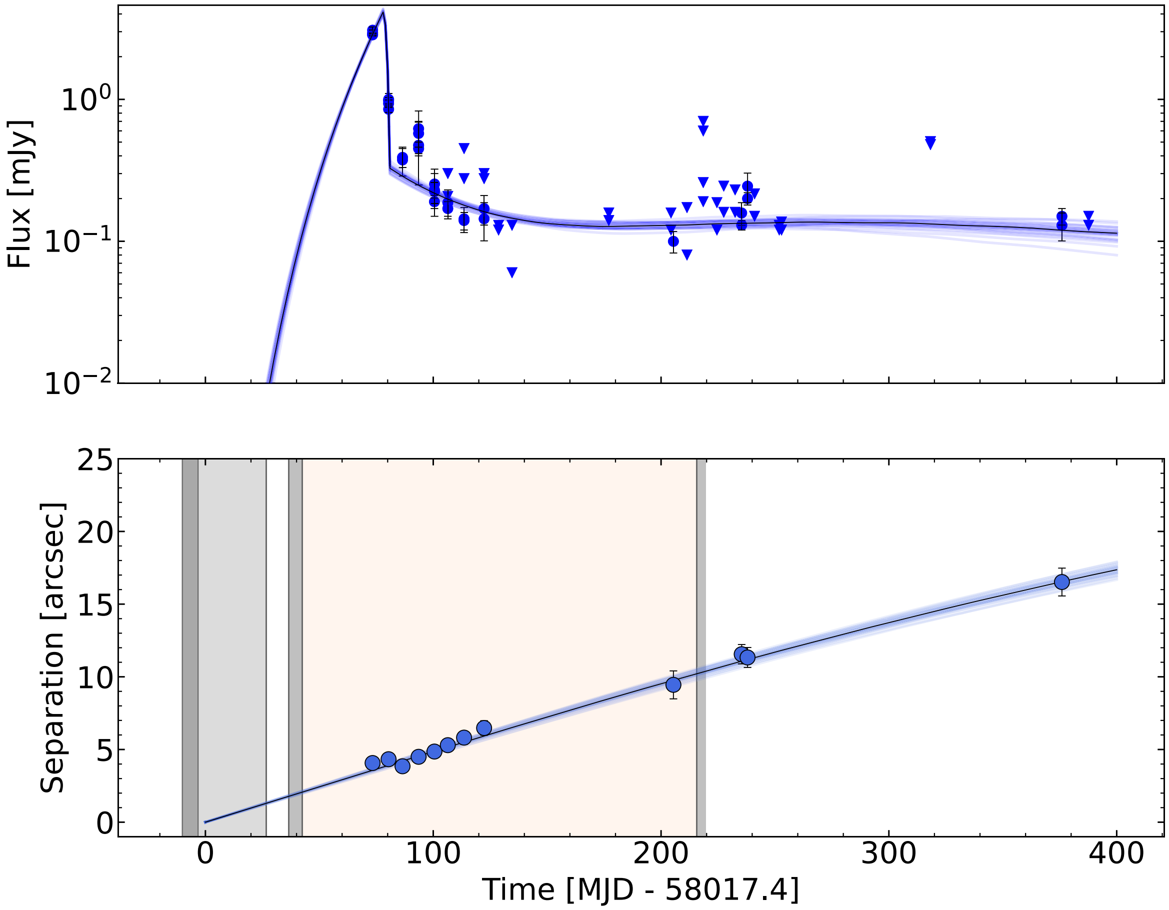

Figure C1. Model (A) light curve (data and model scaled to 5.5 GHz assuming $\alpha = 0.75$), and kinematics obtained from a sample of the posterior parameter distribution.

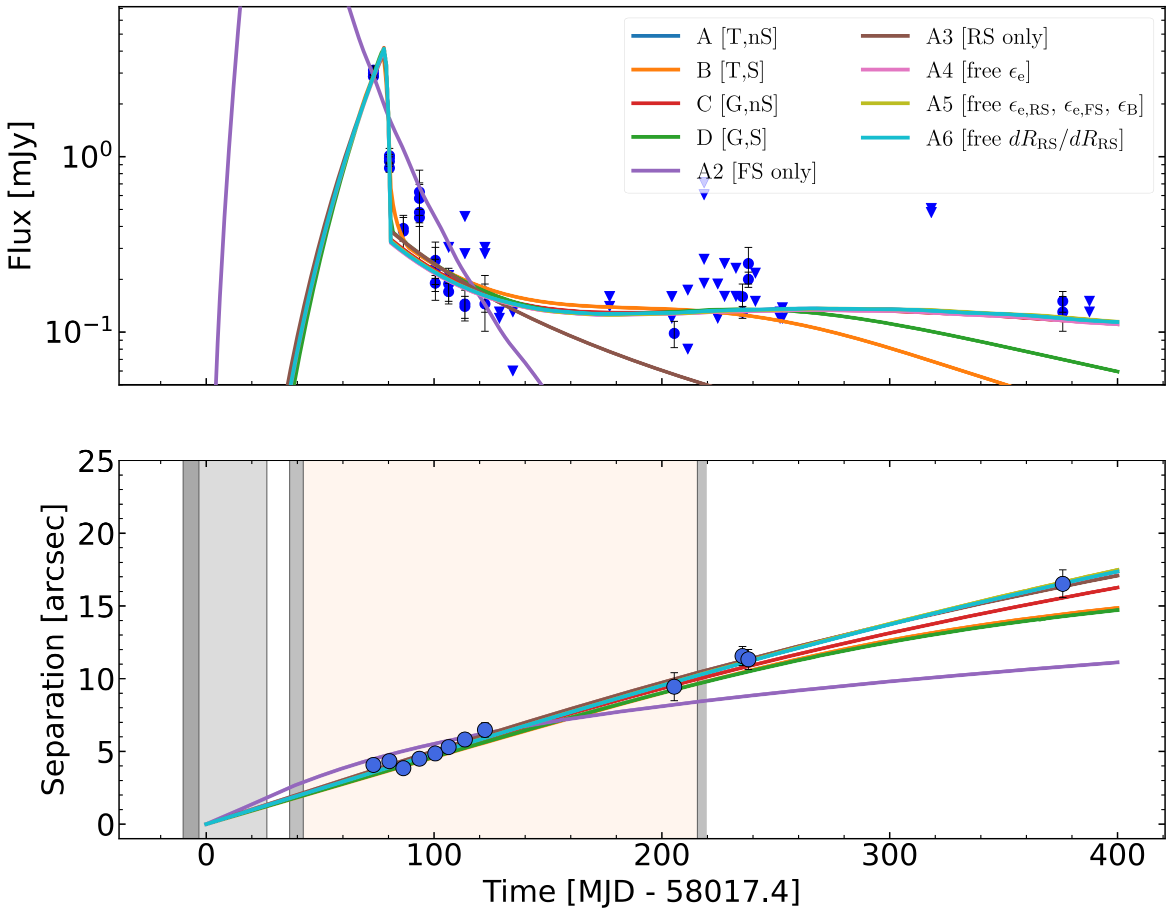

Figure C2. Best-fitting light curves (data scaled to 5.5 GHz assuming $\alpha = 0.75$, irregardless of the best-fiting p for individual models) and kinematics for all models.

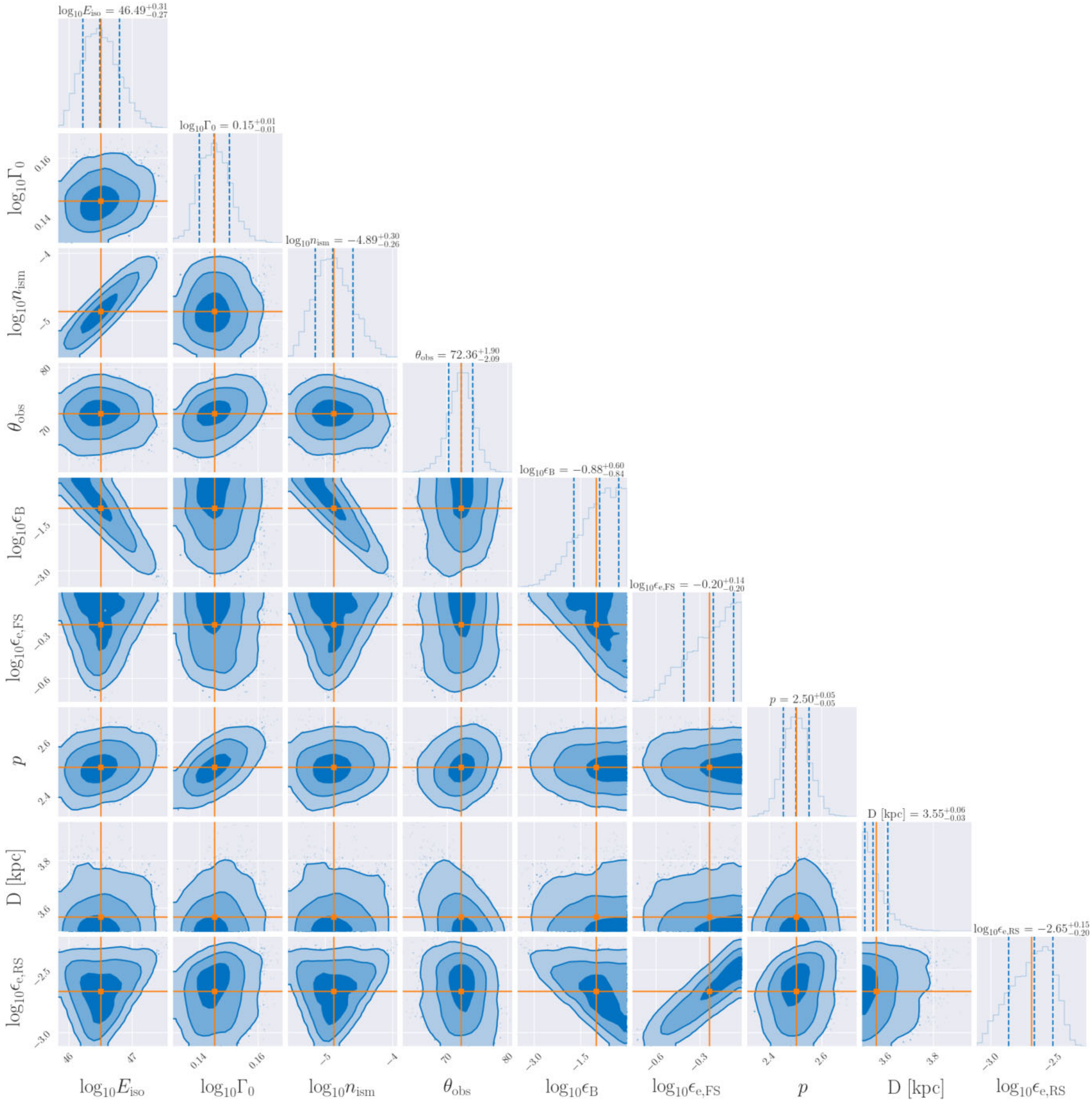

Figure C3. Corner plot of the posterior distributions for Model (A5), the model which had the best reduced χ^2.

This paper has been typeset from a TEX/LATEX file prepared by the author.